Formation of structured membranes by coacervation of xanthan gum with CnTAB surfactants

Keshavarzi, B.; Schwarzenberger, K.; Huang, M.; Javadi, A.; Eckert, K.;

Originally published:

September 2019

Langmuir 35(2019)42, 13624-13635

DOI: https://doi.org/10.1021/acs.langmuir.9b02220

Perma-Link to Publication Repository of HZDR:

https://www.hzdr.de/publications/Publ-29483

Formation of structured membranes by coacervation of xanthan gum with C_nTAB surfactants

Behnam Keshavarzi [†‡§], Karin Schwarzenberger [†,‡], Mengyuan Huang [†,‡], Aliyar Javadi [†,‡,§*], Kerstin Eckert [†,‡*]

[†] Institute of Fluid Dynamics, Helmholtz-Zentrum Dresden-Rossendorf, Bautzner Landstrasse 400, 01328 Dresden, Germany

[‡] Institute of Process Engineering and Environmental Technology, TU Dresden, 01062 Dresden, Germany

[§] Institute of Petroleum Engineering, Chemical Engineering Department, College of Engineering, University of Tehran, Iran

Graphical abstract

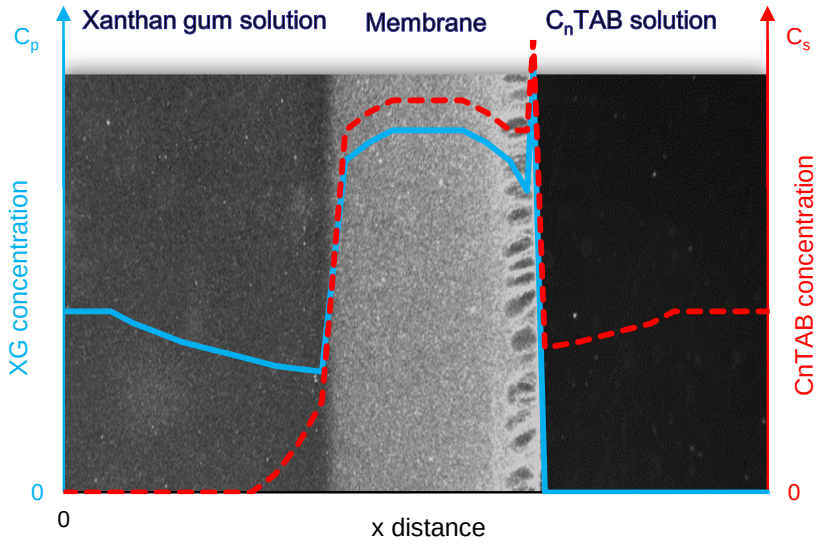

Abstract

We present a novel approach for studying membrane formation by interaction of polymers and surfactants with opposite charge using a Hele-Shaw experimental setup. A solution of the anionic biopolymer xanthan gum is placed in direct contact with a C_nTAB surfactant solution (n=10, 12, 14 and 16). Thereby, a polymer-surfactant membrane spontaneously forms between the two solutions due to the precipitation of polymer-surfactant complexes, which grows afterwards in direction of the polymer solution. The dynamics of the growth of the membrane thickness and the

mass transfer of polymer are evaluated for different surfactant types and concentrations.

The experiments and supporting numerical calculations indicate that polymer mass transfer is driven by diffusion of the charged macromolecules along the concentration gradient which is coupled to the electric field induced by the faster diffusion of the more mobile counterions. The properties and structure of the formed membrane significantly depend on surfactant hydrophobicity and concentration. In addition, in a wide range of experiments, the formation of a porous structure in the membrane is observed whose characteristics can be tuned by the process parameters. A mechanism is proposed for the pore formation explaining it as an instability of the growing membrane surface in interaction with the supply of polymer across the depleted zone in the vicinity of the membrane front.

Keywords: Polymer-surfactant interaction, structure formation, Hele-Shaw, membrane

1 Motivation

The coexistence of polymers and surfactants in an aqueous solution leads to a wide variety of interactions[1], specifically when polymer and surfactant bear opposite charges[1-3]. This case is referred to as “strongly interacting” systems in which attractive electrostatic forces are responsible for attaching surfactant molecules to the polymer chains. In such systems, surface-active polymer-monomer complexes turn into non-surface active polymer-micelle complexes by increasing the surfactant concentration above a certain level at constant polymer concentration. Consequently, a plateau or even a rise in the surface tension isotherm is observed[4-8]. This is accompanied by a precipitation of polymer-surfactant complexes in the solution[3, 9]. The precipitation is termed both coacervation[2-3, 9] and phase separation[4] of polymer-surfactant complexes from the main aqueous phase leading to the formation of a concentrated (polymer-rich) and a dilute (polymer-lean) phase[4]. According to previous reports [3, 10], precipitation appears when the polymer chain takes up enough

surfactants to become stoichiometrically neutralized, i.e. the available charge sites on the polymer chain are progressively occupied by surfactant ions or the polymer counterions. The neutralized complexes then grow by aggregation and self-association and precipitate out of the solution[9]. In some cases, re-dissolution occurs by addition of further surfactant, but in the case of high polymer charge density, the precipitates remain insoluble[1].

Coacervation can be used to produce membranes with different permeabilities [11-16], making it attractive for technological applications like encapsulation or separation processes. Until now, many works have characterized the behavior of oppositely charged polymer-surfactant systems using miscellaneous techniques including surface tension[4-9, 17-21] and surface elasticity measurements[18-20], potentiometry[17], viscometry[9-17], neutron reflectometry[4,22], conductometry[9,21], microcalorimetry[9, 21] and turbidimetry[21]. Yet, the mentioned techniques are mainly based on the analysis of solution properties but do not provide any information about the process of membrane formation.

In this work, the structure and the growth dynamics of the developing polymer-surfactant membrane (PSM) has been observed in-situ for the first time by using the quasi 2D-geometry of a Hele-Shaw cell. By a combination of experiments and numerical simulations, we can link the membrane properties for different surfactant chain lengths and concentrations to the underlying mass transfer and structure formation processes. This in-depth understanding forms the basis to control the tunable membrane properties.

2 Experimental setup and procedure

Xanthan gum (XG) as anionic polymer (i.e. polyelectrolyte) and alkyltrimethylammonium bromide (C_nTAB) as cationic surfactants were provided by Sigma Aldrich. Pre-determined amounts of XG powder and water were weighted in a beaker and then dispersed using an IKA

Ultra Turrax T25 rotor-stator homogenizer (20 minutes, 5000 rpm) to ensure a reproducible sample preparation. Surfactant solutions were prepared by stirring and mixing in an ultrasonic bath. To calculate the critical micelle concentration (CMC) of the surfactants, electrical conductivity measurements were performed (MultiLab-540, WTW). The parameters of the surfactants are given in Table 1. Since pH can affect the charge of the polyelectrolyte XG, we measured the pH values of the employed solutions. For the 3 g/l XG solution, a pH of 5.7 was obtained. Surfactant solutions were used with different concentrations. However, in all cases, the pH was in the range of 5-6. Hence, we assume an approximately constant degree of dissociation for XG.

Table 1. Molecular weight (MW) and critical micelle concentration (CMC) of the C_nTAB surfactants

	MW (g/mol)	**CMC (mM)**
C_{10}TAB	280.29	63.83
C_{12}TAB	308.34	14.94
C_{14}TAB	336.39	3.76
C_{16}TAB	364.5	0.91

The Hele-Shaw experimental setup is depicted in Figure 1. A specifically cut PTFE sheet with a thickness of 0.5 mm is inserted as a spacer between two glass plates (held together by a metal frame) and thus sets a gap width of 0.5 mm. The fluids can be injected into the Hele-Shaw cell through inlet bores, which are connected to filling tubes by PTFE plugs. The gap width is considerably smaller than the length (70 mm from inlet to inlet) and lateral width of the cutout (23 mm at the position of the interface between both solutions). Thus, the cell can be assumed as quasi two-dimensional. The orientation of the Hele-Shaw cell is horizontal, i.e. the gravity vector is perpendicular to the quasi 2D cell. More details on the design of the Hele-Shaw cell can be found elsewhere[23]. For each experiment, the surfactant solution was injected up to the middle of the cell

where it is pinned at the lateral edges of the PTFE sheet. Then the polymer solution was injected to contact the surfactant solution and afterward the growth of the PSM was recorded by a CCD camera (Dalsa DS-21-02M30, 1600 × 1200 pixels, run with 2 × 2 binning and a frame rate of 2 Hz). According to the observations, the flow in the bulk fluid ceases until 10 seconds after the XG injection stops. Slight convection after the filling can be due to pressure equalization when trapped bubbles are present in the exhaust channels in some of the experiments. A LED light source (Imaging Solutions) was used for illumination. Since the XG macromolecules have a size in the order of microns[24-26], their scattered light appears as bright dots in the recorded images. This allows us to track their movement in the fluid layer and hence to quantify the mass transfer of XG toward the membrane. Furthermore, the regions of XG depletion can be identified as darker areas in the recorded images. Each of the Hele-Shaw experiments was repeated to ensure reproducibility of the results.

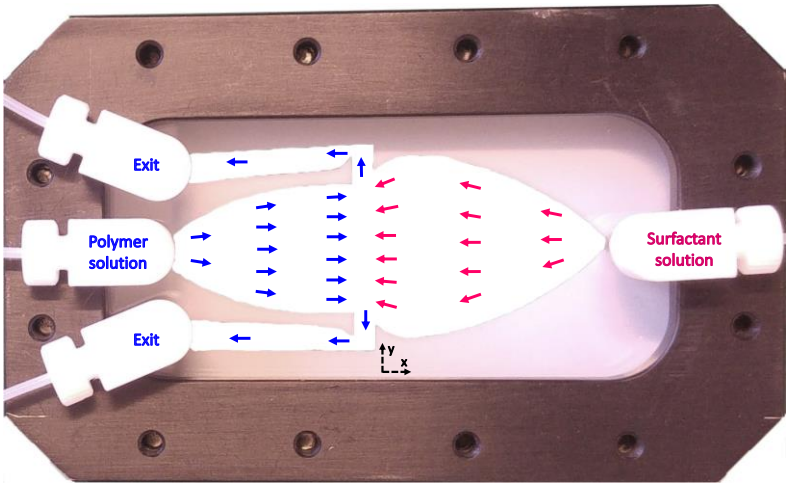

Figure 1. Hele Shaw cell geometry as used in the experiments with schematic representation of flow during filling

3 Results and discussion

3.1 Polymer-surfactant membrane formation and growth in Hele-Shaw cell

As stated previously, a membrane is formed immediately at the beginning of the experiment as a result of the precipitation of polymer-surfactant complexes. The binding of the cationic surfactant to the anionic polymer (polyelectrolyte) reduces the electrostatic repulsion between the charged polymer chains and hydrophobizes the initially hydrophilic XG. This induces agglomeration and phase separation (coacervation) of the hydrophobic polymer-surfactant complexes at the interface between both solutions. Due to the absence of convective mixing in our set-up, concentration gradients evolve at the reaction front. The ensuing mass transfer processes bring further XG and surfactant into contact in the boundary layer adjacent to the membrane. The short distances to the membrane and the absence of convective re-distribution facilitate the agglomeration of the complexes with the membrane. Hence, the membrane grows in thickness towards the polymer solution in the course of the experiment. The developing membrane is like a soft tissue, which can be easily removed from the Hele-Shaw cell after opening the cell. Figure 2 depicts the PSM growth for 3 g/l XG solution and different C_{12}TAB concentrations. The PSM cannot develop in the direction of the surfactant solution because that would require penetration of XG macromolecules through the membrane, which is prevented by their large size. However, the smaller surfactant molecules can diffuse through the PSM and come in contact with non-precipitated polymers. The interaction between the polymer and the surfactant molecules depending on surfactant concentration is described by the surfactant binding isotherm[4-8]. The critical aggregation concentration (CAC) is a characteristic point of the binding isotherm, which gives the minimum surfactant concentration for beginning polymer-surfactant complex formation. Above CAC, the amount of bound surfactant increases until the polymer is saturated at a certain surfactant

concentration (polymer saturation point - PSP). The free surfactant molecules are present as monomers. However, if the local free surfactant concentration exceeds CMC, monomers in a concentration of approximately CMC are coexisting with micelles in a local equilibrium. According to this, free micelles only can be present if the polymer is saturated by surfactant.

Hence, the surfactant concentration plays an important role in the structure of the PSM and its growth rate, defined as the change of the PSM thickness with time $\frac{dL_{PSM}}{dt}$. A smooth membrane is observed for 10 mM C_{12}TAB while coarse pores are created at 40 mM accompanied by an enhanced PSM growth rate. When the surfactant concentration is raised to 80 mM, the growth rate does not change significantly but a higher number of fine pores forms. Figure 3 depicts the changes of PSM thickness in time.

For obtaining the PSM thickness at each time step (as provided in supporting information), a Gaussian smoothing function was applied to each frame to reduce the noise and details of the image. Then the image was binarized to divide between membrane and non-membrane regions by applying a threshold operation. The membrane thickness was calculated by averaging over the whole image height of the membrane part. All image processing routines were programmed in MATLAB. The error bars exemplary given in Figure 3 indicate the standard deviation of the membrane thickness from the mean value.

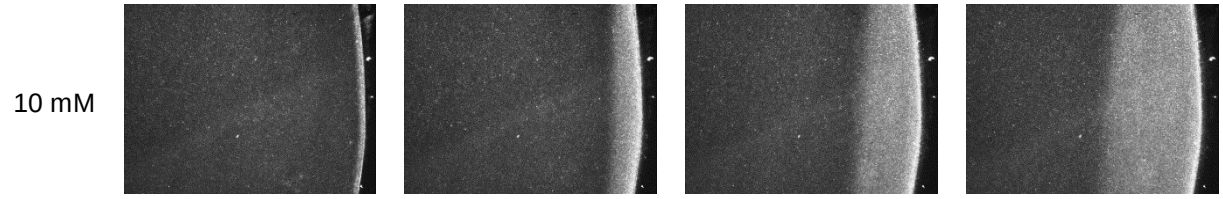

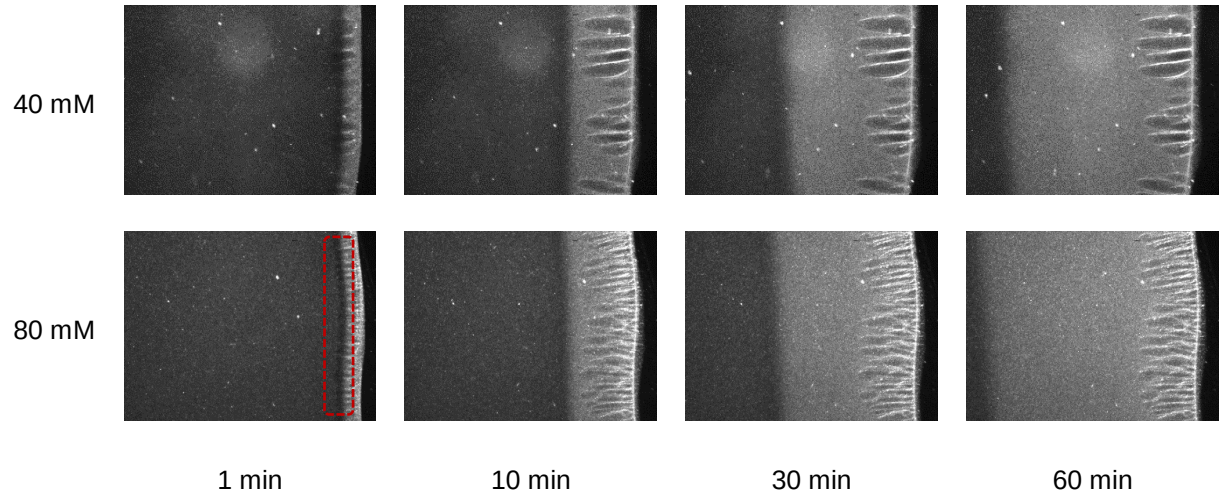

Figure 2. PSM structure development with time for 3 g/l XG concentration and 10, 40 and 80 mM C_{12}TAB concentration. In every picture, the black area at the right edge is the surfactant solution, and the dark area filled with small bright dots at the left is the XG solution. As an example, a zone of strong XG depletion is illustrated as a dark region surrounded by a red rectangle for the case of 80 mM-1 min. The growing dense, white-grey area is the PSM. The pores are darker areas within the PSM. Length and width of the images are 3.0 mm and 2.3 mm, respectively.

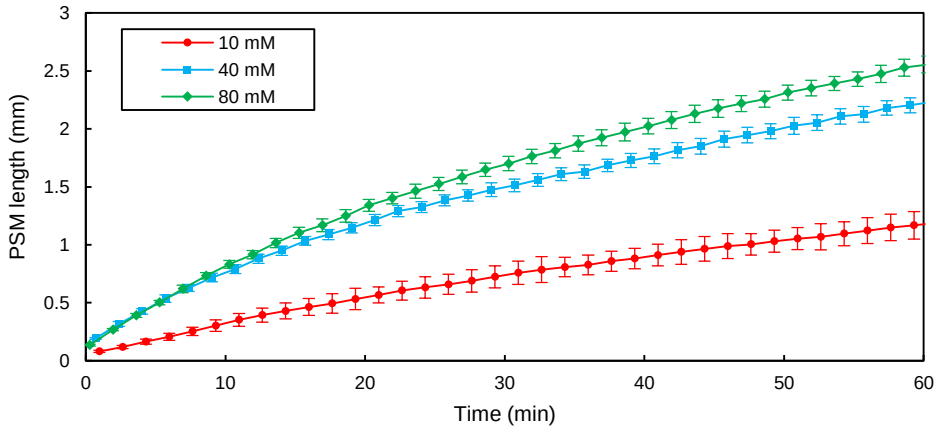

Figure 3. PSM thickness vs. time for 3 g/l XG concentration and different C_{12}TAB concentrations.

The results of Figure 3 demonstrate a direct relationship between PSM growth rate and surfactant concentration. However, the relation is not linear. This can be understood by considering the mass transfer processes in the system since the permeation through the membrane declines with increasing membrane thickness. This leads to a retardation of the PSM growth in Figure 3. Furthermore, at low surfactant concentration, the supply of surfactant through the membrane limits the formation of PSM, resulting in a small growth rate. When the surfactant concentration is high

enough, the PSM growth initially is limited by the supply of XG, which restricts a further acceleration of membrane growth at 80 mM C_{12}TAB compared to 40 mM. This limitation can cause the coinciding curves for 40 mM and 80 mM C_{12}TAB at early times ($t < 10$ min) even if the supply of XG is not necessarily of the same magnitude, because the XG concentration in the membrane also varies with the surfactant concentration (cf. SI, Figure 4 and 5). At later times, the mass transfer resistance of the membrane discussed above again reduces the PSM growth rate, first for 40 mM and later for 80 mM surfactant concentration.

Furthermore, the development of different PSM structures observed in Figure 2 can be explained by this combined mass transfer. In the case of excess XG at low surfactant concentration, a smooth PSM is formed. When the supply of surfactant is high, XG is consumed rapidly generating a depletion zone near the membrane which cannot be compensated by the supply from the XG bulk solution. The depletion zone can be observed as a dark area just at the left of the PSM front in which the number of bright dots representing XG is strongly reduced for the cases of 40 mM and 80 mM at 1 min (example marked as red dashed rectangle in Figure 2). Under these circumstances, a porous structure forms. This probably is caused by an instability of the developing membrane surface described in the following. Consider a small disturbance in membrane thickness, such that a point on the membrane surface reaches slightly wider into the XG depletion zone. The supply of XG from the bulk solution is facilitated at this point compared to the surrounding since the distance to the XG bulk solution is slightly lower there. This amplifies the small initial disturbance meaning that further polymer-surfactant complexes preferably form at this position. This mechanism is analogous to a diffusive instability[27] where the scale of the pattern is determined by the competing effect of the driving force, i.e. the concentration gradient, and interfacial tension which tends to smooth small-scale structures in the surface[27]. With higher driving force, i.e. stronger XG

depletion, the wavelength of the porous structure decreases as shown by the snapshots at 40 mM and 80 mM surfactant concentration in Figure 2 which agrees with the concept of diffusive instability. It should be noted that in our experiments, not classical diffusion is present, but diffusion-migration (cf. Section 3.3). Besides, additional interaction forces between the complexes like hydrophobic or depletion attraction can influence the morphology of the formed structures. In the later stages of the experiment, when the availability of surfactant levels down due to the higher membrane thickness, a second smooth part of PSM forms. Therefore, the pore formation is the result of a high availability of surfactant and a low availability of polymer which persists only at the initial stage and does not span over the whole experiment. Since pattern formation often is an interaction of different processes, and our membrane is a soft material with both continuous and particle-network properties, the full picture of pore formation in the membrane is complex and not completely understood yet. Possible contributing mechanisms could be depletion flocculation of the complexes, in the presence of a high micelle concentration in the solution surrounding the complexes, and the ensuing phase separation into a micelle-rich solution and a polymer-rich phase. Both flocculation and phase separation lead to pattern formation with fractal structures in the first case and more continuous morphologies of spinodal decomposition in the latter case, growing in wavelength by coarsening mechanisms like coalescence and Ostwald ripening. However, due to the pronounced and consistent observation of a XG depletion zone in the porous membrane cases, we believe that the diffusive instability mechanism probably is a main cause for the observed structure formation.

Since the mass transfer of the surfactant considerably influences the membrane formation process, we discuss important aspects of the transport mechanisms in the following. In the surfactant solution at the right hand side of the membrane, only monomers are present at 10 mM

concentration whereas at 40 and 80 mM, both monomers and micelles exist (CMC ≈ 15 mM for C_{12}TAB). Although the micelles are larger than the monomers and have smaller diffusion coefficients, they also may be able to penetrate the membrane depending on the pore size of PSM. In that case, different species including free surfactant monomers, XG-bounded monomers, or XG-bounded micelles and free micelles [28-29] exist in the membrane. Micelles and monomers diffuse individually but a local equilibrium is expected in regions where the free surfactant concentration exceeds CMC. Under these conditions, the monomer concentration approximately equals CMC. The hindrance of surfactant diffusion by the membrane is much more significant for the micelles compared to the monomers. However, the driving force for monomer diffusion becomes negligible between regions where the surfactant concentration is above CMC so that the surfactant transport in the form of micelles is the dominant mechanism there [28].

The surfactant type influences the PSM development as well. At a fixed surfactant concentration of 10 mM, Figure 4 shows higher growth rates for shorter tail surfactants. However, at this concentration, the surfactant with the shortest chain, i.e. C_{10}TAB, is not able to form a membrane even at long times. The coacervation is a result of the polymer charge neutralization and hydrophobization. For short-chain surfactants, the hydrophobicity of the formed complexes is lower compared to the long-chain surfactants. Furthermore, the tendency of the surfactants to bind at the charged polymer sites decreases for small chain lengths (in analogy to their higher solubility), i.e. a larger part of the surfactant molecules is dissociated from the complexes. Hence, higher C_{10}TAB concentrations are required for membrane formation. Note that C_{10}TAB and C_{12}TAB are below CMC at 10 mM while C_{14}TAB and C_{16}TAB are above (Table 1). A better comparison is possible if concentrations above CMC are used for all surfactants. Figure 5 and Figure 6 show the PSM formation at 3 times the CMC concentrations of each surfactant, which

divulge the impact of surfactant type on membrane structure and growth.

The results imply that the reduced growth rate for long-chain surfactants is associated with an increasing PSM compactness, which can be caused by the higher hydrophobicity of the formed polymer-surfactant complexes. A weak pore structure formation sets in for C_{12}TAB and becomes pronounced for C_{14}TAB. However, due to the high PSM compactness at C_{16}TAB, it is unclear whether pores also form in this case or not. Similar to the observations for varying surfactant concentration, the PSM growth rate and structure again are influenced by the supply of surfactant and polymer as detailed in the next section.

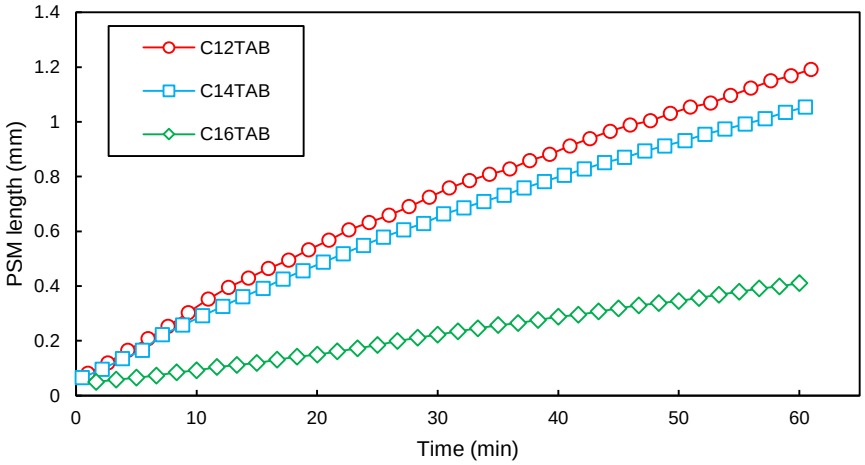

Figure 4- PSM thickness vs. time for 3 g/l XG concentration and 10 mM concentration of different C_nTAB surfactants.

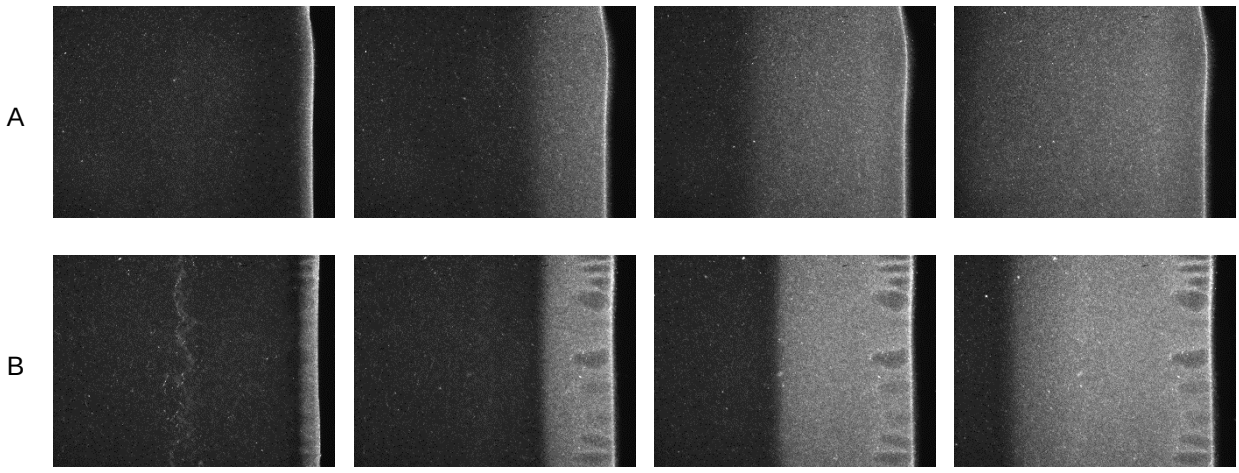

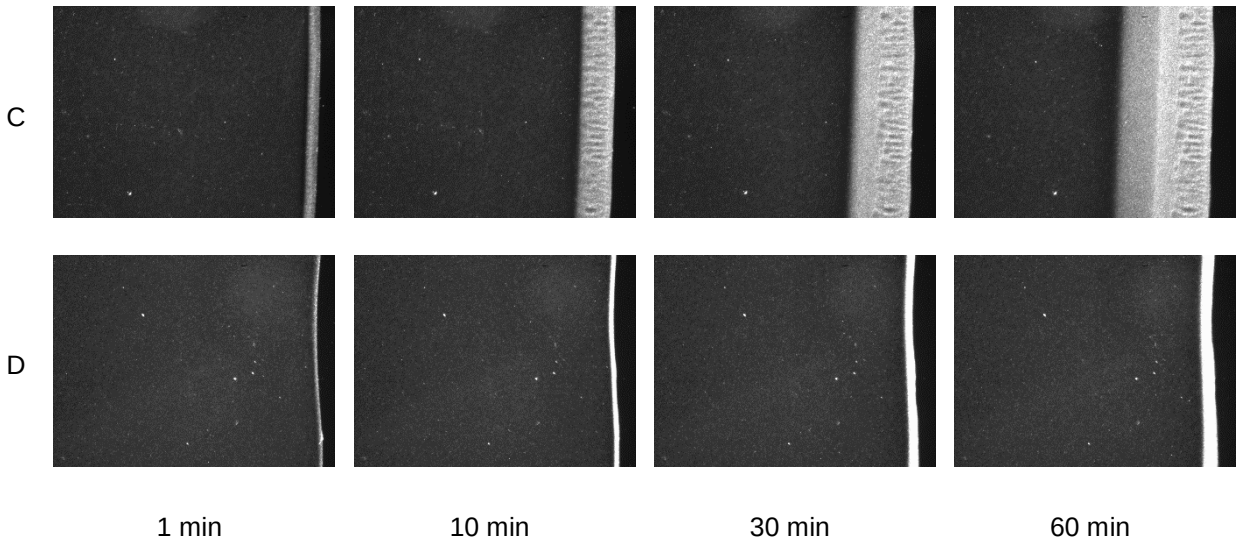

Figure 5. PSM structure development with time for 3 g/l XG concentration and 3 times the CMC concentrations of A) C_{10}TAB, B) C_{12}TAB, C) C_{14}TAB and D) C_{16}TAB. Length and width of the images are 3.0 mm and 2.30 mm, respectively.

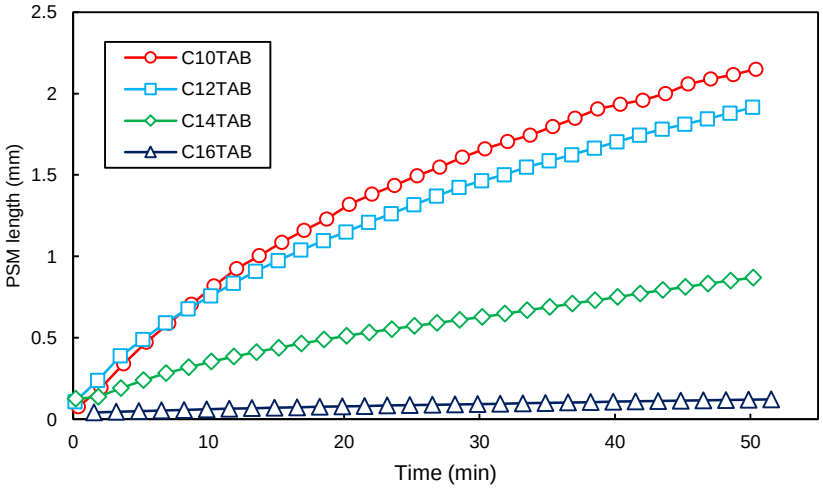

Figure 6- PSM thickness vs. time for 3 g/l XG concentration and 3 times the CMC concentrations of different C_nTAB surfactants.

3.2 Estimation of polymer mass transfer

The mass transfer of XG is characterized by a directional motion of bright dots towards the membrane as visible from the recorded image sequence of the Hele-Shaw experiments (exemplary movies are available in supporting information). This feature, which is discussed later in more detail, is utilized to estimate the XG transfer rates by applying a particle image velocimetry routine (PIVlab[30], available for use in MATLAB) to the XG solution region. This software calculates a

velocity vector field from the cross-correlation of two consecutive images. Figure 7 shows a sample of the obtained velocity plots for 3 g/l XG and 3 times the CMC C_{10}TAB concentration superposed with the binarized image of the PSM. The orange solid curve displays the velocity component in x-direction averaged over the y-direction, i.e. the velocity profile. The velocities are generally less than 2.5 $\frac{\mu m}{sec}$.

For an ideal experiment, only velocity vectors pointing in x-direction would be expected. As indicated in Figure 7, the velocity component sometimes is non-zero in the y-direction. This is due to marginal deviations of the membrane from being parallel to y-axis (as depicted in Figure 1), noticeable in the upper part of the images, which continue in the parts that are not visible in the frame. This deviation creates a slight gradient in the y-direction. However, the magnitude of the y-component is much smaller than the x-component, especially in the near-membrane regions. At the beginning of the experiment, large velocity values are observed in the region near the PSM representing an intense XG mass transfer in the direction of the membrane. In this stage, the velocities are almost zero at the left side of the cell since the concentration gradient is localized in the vicinity of the PSM. Furthermore, there is a notable shift of the membrane position toward the XG solution in the earlier stage of the membrane development. Since this shift is most pronounced for the experiments with high surfactant concentration and low CMC values, it probably is caused by a water exchange between XG and surfactant solutions due to different osmotic pressures at both sides of the membrane. The driving force for the water exchange is highest in the beginning of the experiment where it can affect the mass transfer of XG and surfactant. However, this is only significant for the very initial stage. For the case of 3 times the CMC C_{10}TAB, the speed of the membrane movement already is five times lower than the maximum velocity of the XG particles at t = 2 min, compared to the similar velocities at the start of the experiments. In the later stage,

when the membrane is thick and mechanically stable, no more membrane movement is detectable. The influence of the membrane shift was considered in the calculations of the XG concentration distribution presented in section 3.4.

At later times, the XG concentration gradient gradually propagates through the entire cell. The maximum velocity is also decreasing with time due to the relaxation of the steep initial gradients. This fact together with the reduced surfactant supply across the growing membrane leads to the declining PSM development with time as shown in Figure 3-Figure 6.

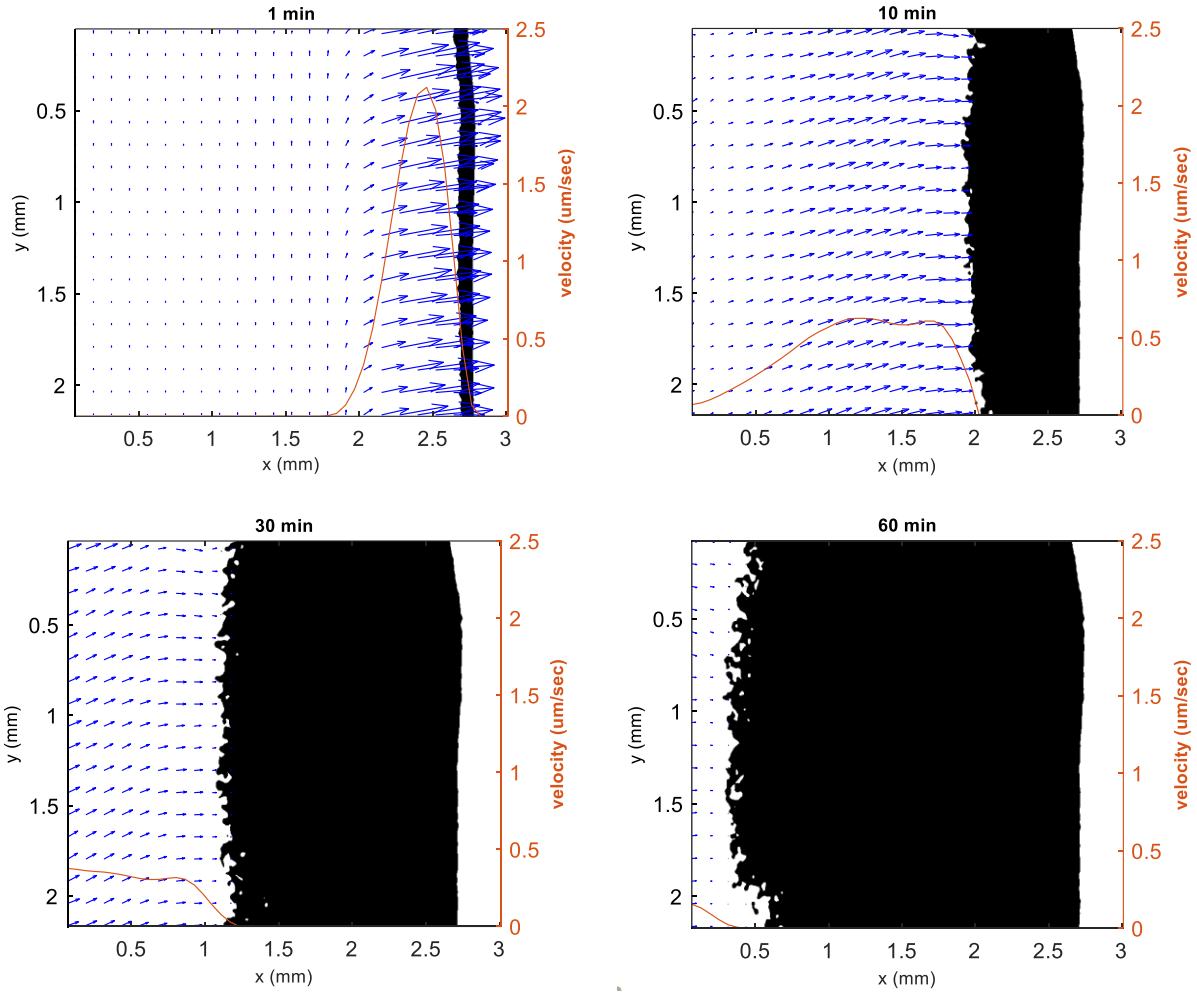

Figure 7. Velocity distribution in XG solution at different times for the experiment with 3 g/l XG and 3 times the CMC C_{10}TAB and profile of horizontal velocity component (orange solid line) superposed to the binarized image of the PSM.

The directional mass transfer of XG has two reasons: (i) the consumption of XG during PSM formation, creating the driving horizontal concentration gradient and (ii) probably the migration of XG in an internal electric field [31-32]. This electric field is generated by the diffusion of the anionic XG, the cationic surfactant and their dissociated counterions along concentration gradients due to their different mass diffusivities (similar to the diffusion potential). In other words, since the small counterions have larger diffusion coefficients, they move faster in the concentration gradient field resulting in a local potential difference. The effect is enhanced when short-chain C_nTAB surfactants are used since in that case the absolute surfactant concentration is higher at 3 times the CMC (according to their higher CMC value). This agrees with the higher velocity magnitudes in the velocity profiles of Figure 8 for short-chain C_nTABs. Nevertheless, the growth in PSM thickness is almost the same in Figure 6 for C_{10}TAB and C_{12}TAB at initial times. This can be explained by the different membrane structures observed. Due to the pore formation in the case of C_{12}TAB, the initial PSM thickness can be similar to C_{10}TAB in Figure 6 even if the XG influx is lower.

The mass flux of XG towards the membrane could be associated with several other effects. Even if the gap width of the horizontal Hele-Shaw cell is narrow, a weak buoyancy-driven convection might develop due to concentration gradients evolving during mass transfer[33]. However, the solutal volume expansion coefficient of XG in water is low[34]. Furthermore, the buoyancy-driven convection would include a backflow of opposite direction in the Hele-Shaw gap. To evaluate the impact of possible buoyancy effects on the mass transfer of XG, we conducted an additional experiment with a vertical orientation of the Hele-Shaw cell to augment the influence of gravity forces. Nevertheless, no considerable change was observed in the results, demonstrating that the influence of buoyancy-driven flow is negligible. Another cause for convection could be the volume

change during the phase separation of PS complexes. By continuity, this flow should extend over the whole liquid domain but it is limited to the vicinity of the membrane in our experimental observations. These facts support the coupled diffusion-electromigration as probable cause for the directional motion of XG. The next sections estimate the mutual influence of diffusion and internal electric field in a XG concentration gradient both experimentally and by a simple numerical model.

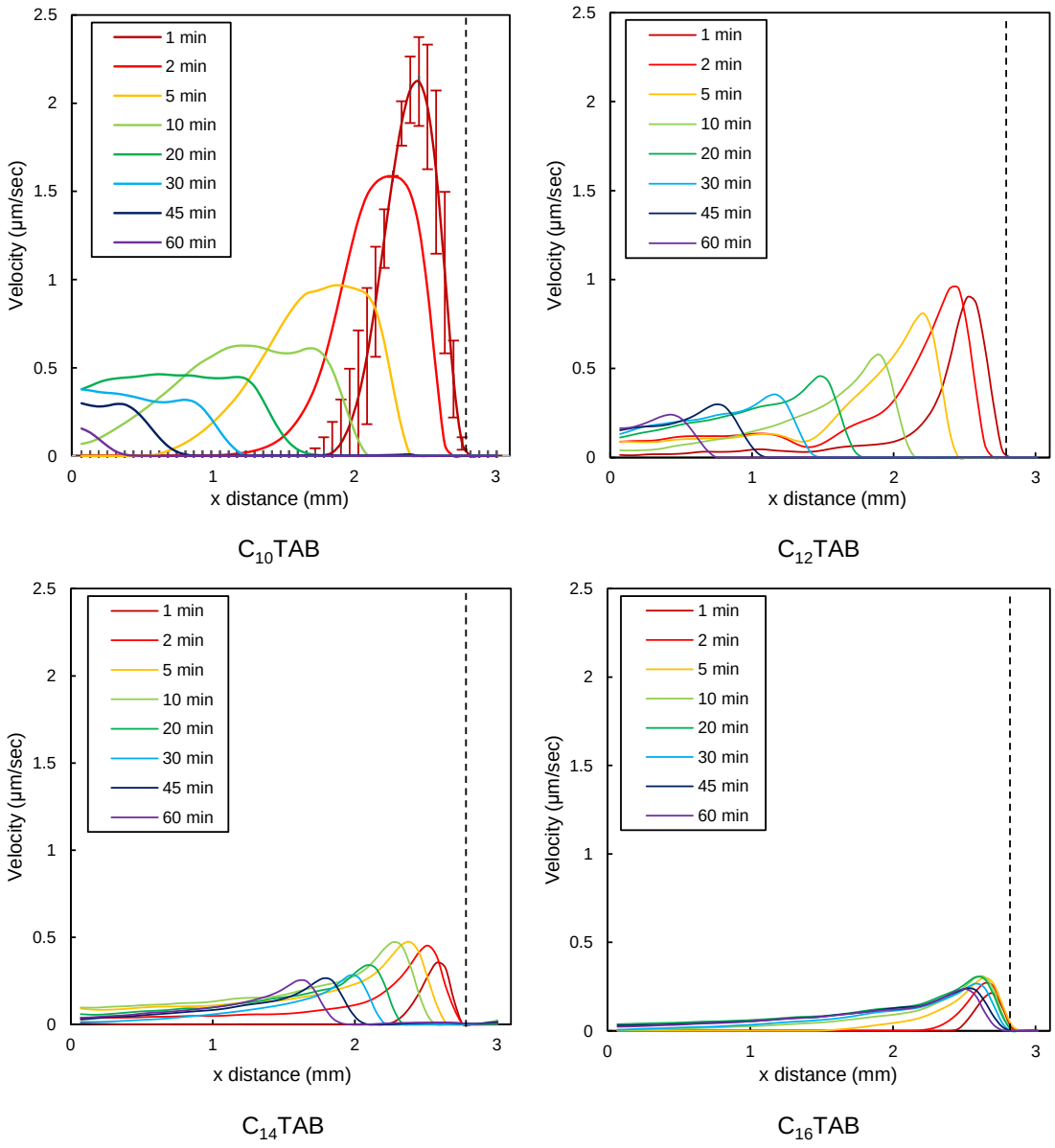

Figure 8. Experimentally determined velocity profiles in XG solution vs. distance for 3 g/l XG and

different surfactants with 3 times the CMC concentrations. The dashed vertical line corresponds to the initial contact line of polymer and surfactant solutions. As an example, the error bars obtained from the standard deviation between three repeated experiments are added to one of the curves in the C_{10}TAB case.

3.3 Diffusion of ionic polymer macromolecules in a concentration gradient

To circumvent the additional complexity of mass transfer across the growing membrane and the consumption of XG by the precipitation, we performed an experiment for the case of diffusive mixing of a 3 g/l XG solution and pure water in the Hele-Shaw cell. The velocity profiles (Figure 9) were obtained by applying the PIV analysis on consecutive images as described previously in section 3.2. The main result of Figure 9 is that both the directional movement of XG is also observed in this case and the velocity magnitudes are in the order of the PSM experiments. To confirm these findings, we implemented a simplified numerical model of the process observed in Figure 9, which is described in the following section.

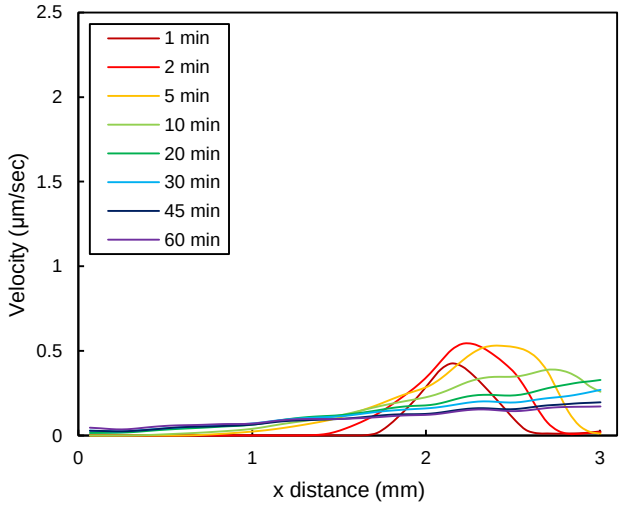

Figure 9. Velocity profile in the polymer solution vs. distance for the diffusion of 3 g/l XG into pure water.

3.3.1 Modeling of XG mass transfer in water

The electric field results from the diffusion of the charged ions and is given by the charge conservation:

$$\boldsymbol{E} = -\nabla\phi \qquad (1)$$

$$\nabla \cdot (\epsilon_0 \epsilon_\mathrm{r} \boldsymbol{E}) = \rho_\mathrm{v} \tag{2}$$

Here E is the electric field, ϕ is the electric potential, ϵ_0 is the vacuum permittivity, ϵ_r is the relative permittivity and ρ_v is the space charge density which takes the following form [35]:

$$\rho_\mathrm{v} = F \sum_i z_i \, c_i \tag{3}$$

where F is the Faraday constant given by $F = eN_A = 96485 \frac{C}{mol}$ (with $e = 1.6 \times 10^{-19} C$ – charge of an electron, $N_A = 6.022 \times 10^{23}$ – Avogadro number), z_i and c_i are the charge number and the concentration of species i, respectively. The concentration field is calculated by the Nernst-Planck-equation [36]:

$$\frac{\partial c_i}{\partial t} = z_i F \frac{D_i}{RT} \nabla \cdot (c_i \nabla \phi) + D_i \Delta c_i \tag{4}$$

Where D_i denotes the diffusion coefficient of species i, R is the universal gas constant and T is the absolute temperature. The first and the second terms on the right hand side of Eq. (4) denote the migration due to the electric field and the diffusion, respectively. Note that this model neglects the colloidal properties of the XG macromolecule for a simplified coupling to the diffusion of the small counterions.

3.3.2 Numerical setup

As shown in Figure 10, a simplified one-dimensional model with two species was adopted. Species 1 and 2 denote the anionic XG macromolecule (average MW of $2 \times 10^6 \, g/mol$) and its positively charged counterion. According to the literature, XG has two dissociable counterions per monomer, which can be Na^+, H^+, K^+ and Ca^{2+} [25-26, 37-39]. For the sake of simplicity, we assumed Na^+ as the representative counterion. For an accurate simulation, the knowledge of the XG dissociation rate is required. As a rough estimation, we assumed $z_1 = -2000$ (corresponding to a charge number of -1 per monomer with a MW of $1000 \, g/mol$, which is close to reality [37]) and $z_2 = +1$. The

domain is divided into two parts. The initial concentrations of XG and the counterion are 1.5×10^{-6} M (equivalent to 3 g/l XG concentration) and 3×10^{-3} M on the left and zero on the right side. The diffusion coefficients [26] are assumed to be constant values of $D_1 = 3.2 \times 10^{-12}\ m^2/s$ (diffusivity of the XG macromolecule) and $D_2 = 1 \times 10^{-9}\ m^2/s$ (diffusivity of Na^+). As species 2 diffuses much faster than species 1, it is expected that the transport of species 2 to the right side will enhance the electric potential in this region, resulting in an electric field which will augment the migration transport of species 1. For comparison, an additional simulation of the species transport was conducted where the electric field is neglected.

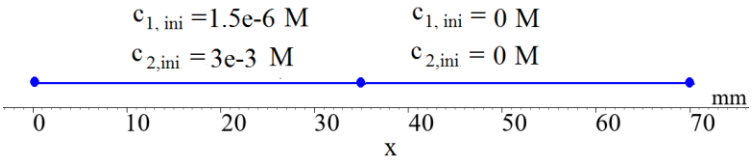

Figure 10. Simplified one-dimensional model as used in the simulations with two species: the XG macromolecule and its counterion Na^+, which are initially located in the left part of the domain ($0 \leq x \leq 35\ mm$).

3.3.3 Simulation results

The electric potential at different time instants is shown in Figure 11. At the beginning of the process, the electric field is extremely strong as the concentration gradient and the associated diffusive transport of species 2 is very high. With the ongoing process, the electric field is weakened due to the migration transport of both species.

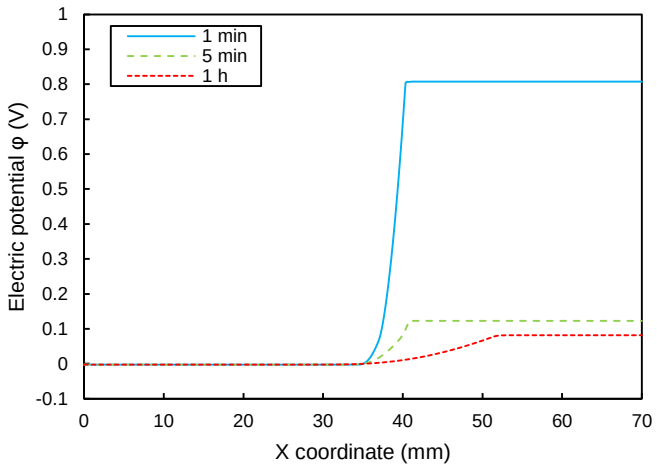

Figure 11. Electric potential ϕ at times of 1 min, 5 min, and 1 h.

Figure 12 shows the flux of XG with and without electric field. In general, the flux at the beginning of the process is much stronger than in later stages, which corresponds to the high concentration gradient and the high electric potential at the beginning. The electric field enhances the polymer flux to about 15 times at the beginning and later stages of the process. Such a significant increase agrees with the observations in literature [40]. In view of the strong simplifications inherent in our numerical model, this value rather provides a rough order of magnitude than a quantitative comparison. For example, the spatial extension of the XG macromolecules is not included in our model, as well as concentration dependencies of the XG conformation and diffusion coefficients. The modeling and simulation of the process in presence of the surfactant solution is even more complicated and requires consideration of the mass fluxes of surfactant ions and counterions, the surfactant monomer-micelle equilibrium as well as incorporating the precipitation of polymer-surfactant complexes according to the binding isotherm. The precipitation not only changes the polymer and surfactant concentration but also forms a porous membrane with varying porosity and permeability again influencing the mass transfer processes of surfactant monomers and micelles. An example for these complex interdependencies is discussed in Sec. 3 of the SI.

However, the numerical results provide instructive insights into the contribution of the internal electric field to the mass transfer of polymers. In the polymer-surfactant case, it can be expected that the difference in diffusivities of surfactants and their counterions further amplifies the electric field. The consumption of polymers and surfactants at the front maintains high concentration gradients what furthermore intensifies the mass transfer. This explains the large velocity values for the cases reported in Figure 8.

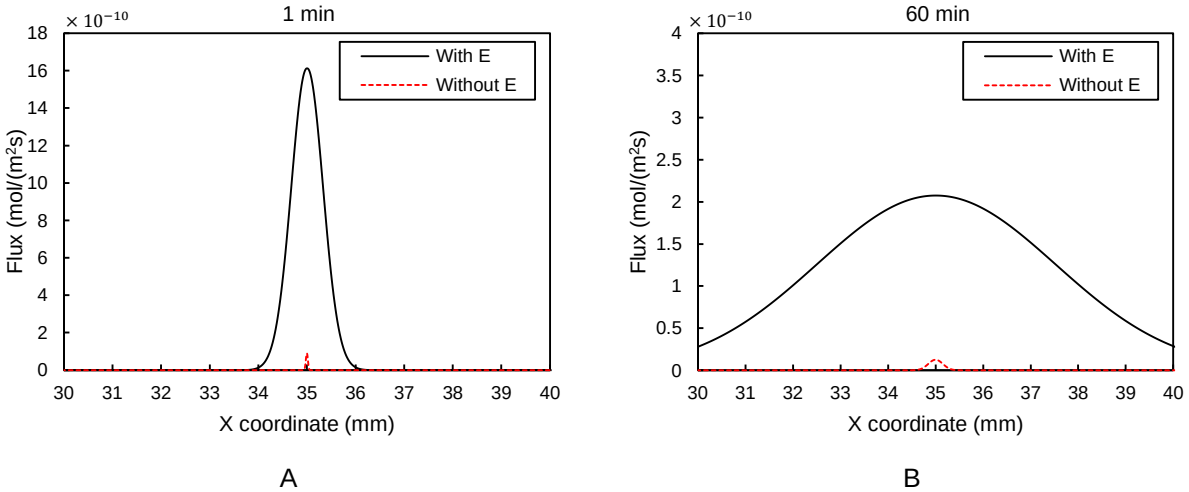

Figure 12. Flux of XG with and without electric field *E* at times of A) 1 min and B) 60 min.

3.4 XG concentration distribution

According to Figure 5, the different surfactant chain lengths lead to varying compactness of the PSM. The velocity profiles obtained in Section 3.2 now allow us to roughly quantify the local concentration of XG in the membrane as well as in the polymer solution. This procedure is more robust than directly correlating the PSM compactness to the brightness information from the images. Since the illumination is newly adjusted with each run, the brightness may change slightly from one experiment to another. For estimating the time-dependent XG distribution, a homogeneous XG concentration of 3 g/l in the solution was considered as initial condition, marked as a horizontal red line in Figure 13. Furthermore, a one-dimensional flow of XG in x direction

was assumed. To obtain the polymer flux in the x direction, we used the horizontal velocity components (cf. the profiles in Figure 8). The Hele-Shaw cell was discretized in x direction with a grid size determined by the resolution of the vector field as displayed in Figure 7. The concentration in each grid cell was updated in every time step by the inflow from and the outflow to the adjacent grid cells. Since the inflow and the concentration of the leftmost cell were not given by this analysis, they both were approximated by a linear extrapolation of the three neighboring cells. Different extrapolation schemes were tested but yielded similar results due to the smooth gradients in this part of the experimental domain. The time step corresponds to the frame rate of the image processing, 0.1 Hz, which is appropriate to capture the slow dynamics in the phase of membrane growth. The short initial phase however is characterized by a highly transient evolution and very fine structures in the concentration field. Besides, the moment of contact of both solutions coincides with the filling procedure. In this stage, a thin, dense membrane layer facing the surfactant solution instantaneously forms for all studied surfactant chain lengths in Figure 5. This feature therefore is not represented in Figure 13. The depletion zone in the polymer solution and the elevated XG concentration within the PSM are observed for all surfactant chain lengths. Furthermore, the pore structure appears as decreased XG concentration at the right side of the membrane ($x > 2.5$ mm) for C_{12}TAB and C_{14}TAB. A marked increase of the XG concentration within the PSM compared to the initial XG concentration however is only obtained for long-chain C_nTABs. For short-chain C_nTABs, the PSM consists of a rather loose network of polymer-surfactant complexes on account of their lower hydrophobicity. Moreover, the larger degree of dissociation of surfactant ions from the complexes for short-chain C_nTABs yields a higher ionic strength in the PSM and thus a larger water content of the membrane at equilibrium. Hence, we can expect a higher membrane permeability in those cases.

The compact XG accumulation for long-chain C_nTABs points to low membrane permeability, and accordingly to a reduced mass transfer of surfactants across the membrane. This induces a weaker XG delivery as shown by the velocity values depicted in Figure 8 for long-chain C_nTABs. At the same time, a lower surfactant to polymer ratio in the solution is needed for the long-chain C_nTABs to induce phase separation on account of their higher hydrophobicity. Both effects result in a stronger depletion of XG before the PSM which is confirmed in Figure 13. It is worth mentioning that the higher compactness of membranes formed by the long-chain surfactants is not only a dynamic effect. It is also observed when we produce membrane-like precipitate by mixing polymer and surfactant solutions in a beaker and stir long enough to reach equilibrium.

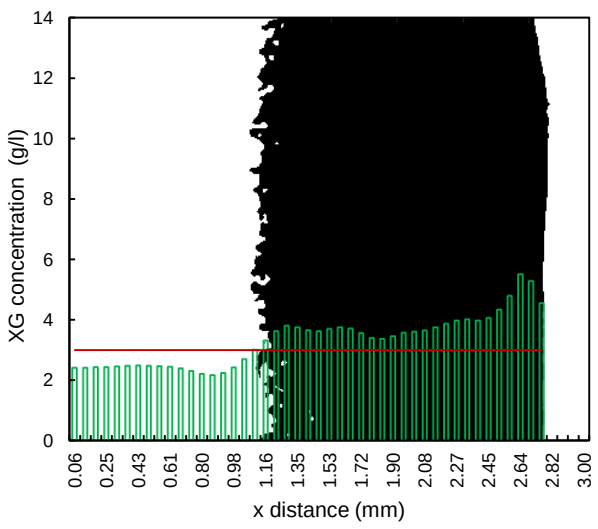

C_{10}TAB

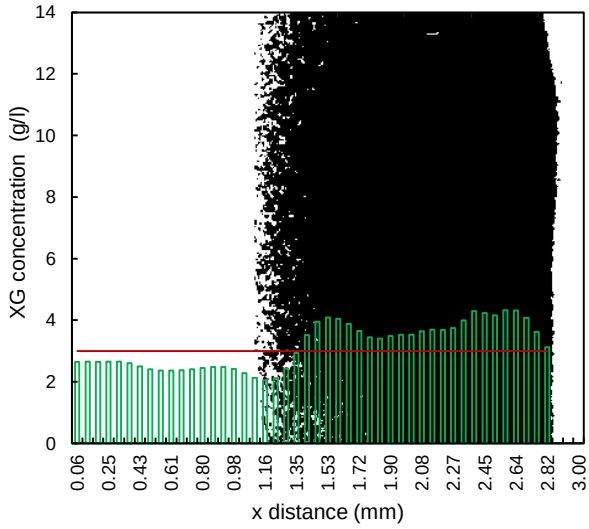

C_{12}TAB

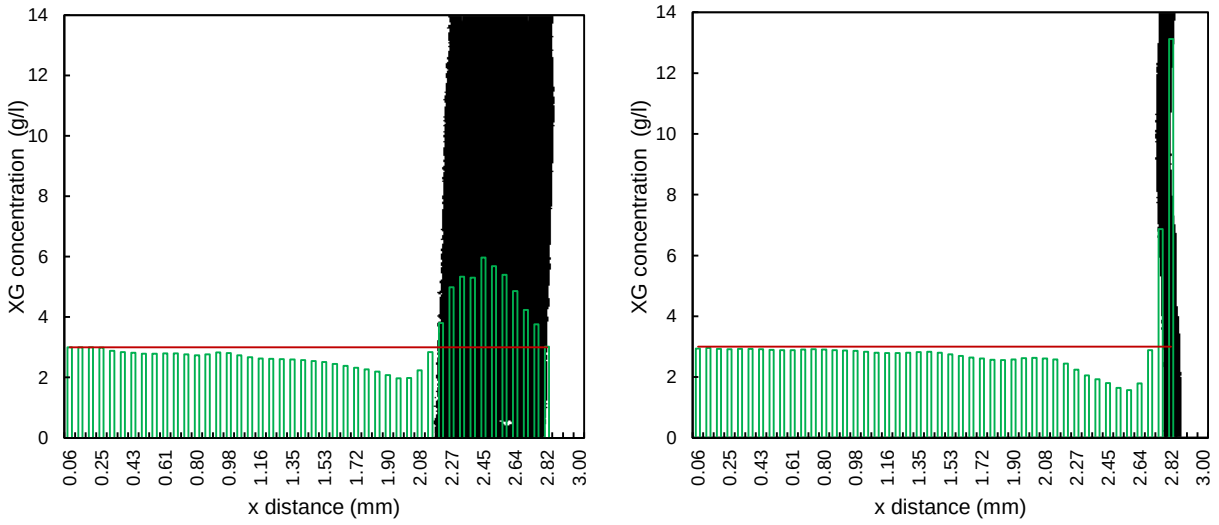

C_{14}TAB C_{16}TAB

Figure 13. Concentration of XG in the cell for different surfactants after 30 minutes superposed with the binarized PSM image. The initial polymer and surfactant concentration were 3 g/l (red line) and 3 times the CMC, respectively.

Considering a spatially constant surfactant-to-polymer ratio in the PSM, we can expect the same concentration profile as XG (as depicted in Figure 13) for the membrane-bound surfactant multiplied by a proportionality constant. In addition, surfactant molecules diffuse through the PSM and further into the XG solution inducing a surfactant concentration gradient in the left side of the membrane. Under conditions where further complex formation is observed, the surfactant concentration starts at a value larger than the critical aggregation concentration in the XG solution near the membrane and reaches zero after some distance in the bulk solution. Figure 14 illustrates a qualitative sketch of the concentration changes through the cell as an aid for a better understanding of the overall mass transfer processes.

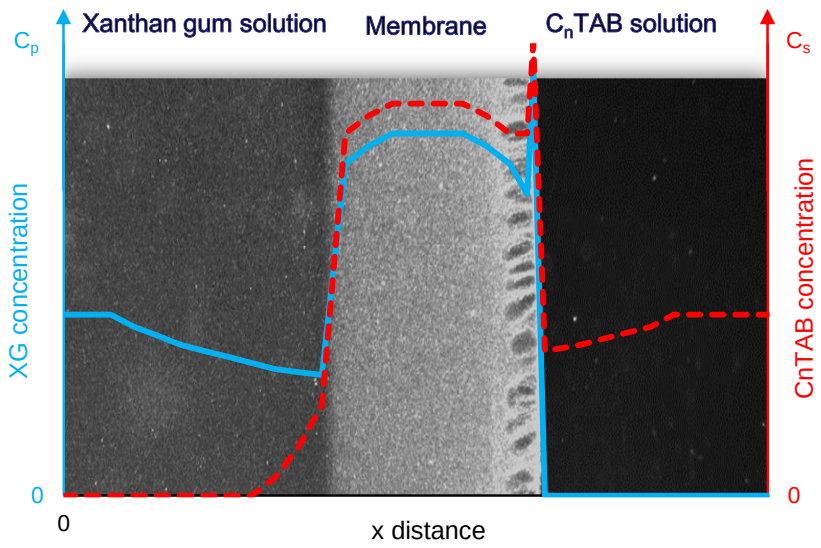

Figure 14. Qualitative description of XG and C_nTAB concentration profiles through the cell.

4 Conclusions

We used a quasi-two-dimensional Hele-Shaw setup to study the formation and growth of a membrane by electrostatic interaction of oppositely charged polymers and surfactants. At the initial contact of the polymer and surfactant solutions in the Hele-Shaw cell, a thin membrane forms spontaneously which separates both solutions. Afterwards, the membrane continues to grow by penetration of surfactants through the membrane and diffusion and migration of polymers from the bulk solution. The migration of polymers in the concentration gradient is accelerated by the consumption of polymers at the front of membrane development as well as the electric field originating from the different diffusivities of ionic polymers, surfactants and their counterions. We further identified the main mechanisms underlying the membrane growth and structure formation by employing different surfactant chain lengths and concentrations. It was revealed that the surfactant hydrophobicity plays an important role as more compact and less permeable structures are formed using longer chain surfactants. Increasing the surfactant concentration leads to thicker

membranes and increases the frequency of pore structures. On this basis, it is possible to tune the membrane thickness, compactness, porosity and pore structure. These properties are essential for technological applications since they determine the selectivity, permeability and mechanical stability of the membrane. The porous structures obtained in this work have the potential to be used as asymmetric membranes providing high mechanical stability and selectivity together with a large specific permeate flux, a concept that already is applied in ceramic membranes.

▪ Associated content

Supporting information

The supporting material contains

- the video files of the membrane development for the cases of 3 g/l XG and 3 times the CMC concentration of C_{10}TAB, C_{12}TAB, C_{14}TAB and C_{16}TAB (video frames are 3 mm length * 2.3 mm width, the playback speed is 300 times faster than real-time),
- the image processing routine to calculate the membrane thickness,
- more information on modeling the mass transfer of XG and its counterion, and
- additional figures for 3 g/l XG and 10, 40 and 80 mM C_{12}TAB tests.

▪ Author information

***Email:** k.eckert@hzdr.de, Tel: +49 351 260 3860

***Email:** javadi.aliyar@ut.ac.ir

Notes: The authors declare no competing financial interest.

▪ Acknowledgments

The authors would like to acknowledge the financial support provided by the German Helmholtz Association, by the Dresden Fellowship Programme of TU Dresden (AJ & KE) and

Deutsche Forschungsgemeinschaft, grant no. MU 4209/1-1 and EC 201/8-1.

References

1. Goddard, E.D. and Ananthapadamanabhan, K.P., 2017. Interactions of Surfactants with Polymers and Proteins. CRC press, Taylor and Francis group.
2. Piculell, L., 2013. Understanding and exploiting the phase behavior of mixtures of oppositely charged polymers and surfactants in water. Langmuir, 29(33), pp.10313-10329.
3. Wang, Y., Kimura, K., Dubin, P.L. and Jaeger, W., 2000. Polyelectrolyte− micelle coacervation: effects of micelle surface charge density, polymer molecular weight, and polymer/surfactant ratio. Macromolecules, 33(9), pp.3324-3331.
4. Bahramian, A., Thomas, R.K. and Penfold, J., 2014. The adsorption behavior of ionic surfactants and their mixtures with nonionic polymers and with polyelectrolytes of opposite charge at the air–water interface. The Journal of Physical Chemistry B, 118(10), pp.2769-2783.
5.Taylor, D.J.F., Thomas, R.K., Hines, J.D., Humphreys, K. and Penfold, J., 2002. The adsorption of oppositely charged polyelectrolyte/surfactant mixtures at the air/water interface: Neutron reflection from dodecyl trimethylammonium bromide/sodium poly (styrene sulfonate) and sodium dodecyl sulfate/poly (vinyl pyridinium chloride). Langmuir, 18(25), pp.9783-9791.
6.Taylor, D.J.F., Thomas, R.K., Li, P.X. and Penfold, J., 2003. Adsorption of oppositely charged polyelectrolyte/surfactant mixtures. Neutron reflection from alkyl trimethylammonium bromides and sodium poly (styrenesulfonate) at the air/water interface: the effect of surfactant chain length. Langmuir, 19(9), pp.3712-3719.
7. Bell, C.G., Breward, C.J., Howell, P.D., Penfold, J. and Thomas, R.K., 2007. Macroscopic modeling of the surface tension of polymer− surfactant systems. Langmuir, 23(11), pp.6042-6052.
8. Bell, C.G., Breward, C.J., Howell, P.D., Penfold, J. and Thomas, R.K., 2010. A theoretical analysis of the surface tension profiles of strongly interacting polymer–surfactant systems. Journal of colloid and interface science, 350(2), pp.486-493.
9. Mukherjee, I., Sarkar, D. and Moulik, S.P., 2010. Interaction of gums (guar, carboxymethylhydroxypropyl guar, diutan, and xanthan) with surfactants (DTAB, CTAB, and TX-100) in aqueous medium. Langmuir, 26(23), pp.17906-17912.
10. Wang, C. and Tam, K.C., 2002. New insights on the interaction mechanism within oppositely charged polymer/surfactant systems. Langmuir, 18(17), pp.6484-6490.
11. Ijichi, K., Yoshizawa, H., Uemura, Y., Hatate, Y., and Kawano, Y, 1997. Multi-layered gelatin/acacia microcapsules by complex coacervation method. Journal of chemical engineering of Japan, 30(5), 793-798.

12. Zorzi Bueno, C., and Maria Moraes, Â., 2011. Development of porous lamellar chitosan-alginate membranes: Effect of different surfactants on biomaterial properties. Journal of Applied Polymer Science, 122(1), 624-631.
13. Barrow, C. J., Nolan, C., and Jin, Y., 2007. Stabilization of highly unsaturated fatty acids and delivery into foods. Lipid Technology, 19(5), 108-111.
14. Keshavarzi, B. Javadi, A. and Bahramian, A. Waste Water treatment, PCT/IB2018/060554, filed on December 22, 2018.
15. Comas-Rojas, H., Aluicio-Sarduy, E., Rodríguez-Calvo, S., Pérez-Gramatges, A., Roser, S.J. and Edler, K.J., 2007. Interactions and film formation in polyethylenimine–cetyltrimethylammonium bromide aqueous mixtures at low surfactant concentration. Soft Matter, 3(6), pp.747-753.
16. Edler, K.J., Goldar, A., Brennan, T. and Roser, S.J., 2003. Spontaneous free-standing nanostructured film growth in polyelectrolyte-surfactant systems. Chemical Communications, (14), pp.1724-1725.
17. Jain, N., Trabelsi, S., Guillot, S., McLoughlin, D., Langevin, D., Letellier, P. and Turmine, M., 2004. Critical aggregation concentration in mixed solutions of anionic polyelectrolytes and cationic surfactants. Langmuir, 20(20), pp.8496-8503.
18. Noskov, B.A., Grigoriev, D.O., Lin, S.Y., Loglio, G. and Miller, R., 2007. Dynamic surface properties of polyelectrolyte/surfactant adsorption films at the air/water interface: Poly (diallyldimethylammonium chloride) and sodium dodecylsulfate. Langmuir, 23(19), pp.9641-9651.
19. Noskov, B.A., Loglio, G., Lin, S.Y. and Miller, R., 2006. Dynamic surface elasticity of polyelectrolyte/surfactant adsorption films at the air/water interface: Dodecyltrimethylammonium bromide and copolymer of sodium 2-acrylamido-2-methyl-1-propansulfonate with N-isopropylacrylamide. Journal of colloid and interface science, 301(2), pp.386-394.
20. Koolivand-Salooki, M., Javadi, A., Bahramian, A. and Abdollahi, M., 2019. Dynamic interfacial properties and foamability of polyelectrolyte-surfactant mixtures. Colloids and Surfaces A: Physicochemical and Engineering Aspects, 562, pp.345-353.
21. Chakraborty, T., Chakraborty, I. and Ghosh, S., 2006. Sodium carboxymethylcellulose− CTAB interaction: a detailed thermodynamic study of polymer− surfactant interaction with opposite charges. Langmuir, 22(24), pp.9905-9913.
22. Campbell, R.A., Yanez Arteta, M., Angus-Smyth, A., Nylander, T. and Varga, I., 2011. Effects of bulk colloidal stability on adsorption layers of poly (diallyldimethylammonium chloride)/sodium dodecyl sulfate at the air–water interface studied by neutron reflectometry. The Journal of Physical Chemistry B, 115(51), pp.15202-15213.
23. Shi, Y. and Eckert, K., 2008. A novel Hele-Shaw cell design for the analysis of hydrodynamic instabilities in liquid–liquid systems. Chemical Engineering Science, 63(13), pp.3560-3563.
24. Camesano, T.A. and Wilkinson, K.J., 2001. Single molecule study of xanthan conformation using atomic force microscopy. Biomacromolecules, 2(4), pp.1184-1191.
25. Iijima, M., Shinozaki, M., Hatakeyama, T., Takahashi, M. and Hatakeyama, H., 2007. AFM studies on gelation mechanism of xanthan gum hydrogels. Carbohydrate polymers, 68(4), pp.701-

707.
26. Southwick, J.G., McDonnell, M.E., Jamieson, A.M. and Blackwell, J., 1979. Solution studies of xanthan gum employing quasielastic light scattering. Macromolecules, 12(2), pp.305-311.
27. Mullins, W. W., and Sekerka, R. F., 1964. Stability of a planar interface during solidification of a dilute binary alloy. Journal of applied physics, 35(2), 444-451.
28. Krovvidi, K.R., Muscat, A., Stroeve, P. and Ruckenstein, E., 1984. Transport of monomer surfactant molecules and hindered diffusion of micelles through porous membranes. Journal of colloid and interface science, 100(2), pp.497-505.
29. Valente, A.J.M., Burrows, H.D., Polishchuk, A.Y., Domingues, C.P., Borges, O.M.F., Eusébio, M.E.S., Maria, T.M.R., Lobo, V.M.M. and Monkman, A.P., 2005. Permeation of sodium dodecyl sulfate through polyaniline-modified cellulose acetate membranes. Polymer, 46(16), pp.5918-5928.
30. Thielicke, W. and Stamhuis, E., 2014. PIVlab – towards user-friendly, affordable and accurate digital particle image velocimetry in MATLAB. Journal of Open Research Software, 2(1).
31. Alexandrowicz, Z. and Daniel, E., 1963. Sedimentation and diffusion of polyelectrolytes. Part I. Theoretical description. Biopolymers: Original Research on Biomolecules, 1(5), pp.447-471.
32. Varoqui, R. and Schmitt, A., 1972. Limiting sedimentation and diffusion coefficients of polyelectrolytes. The charge effect. Biopolymers: Original Research on Biomolecules, 11(6), pp.1119-1136.
33. Köllner, T., Schwarzenberger, K., Eckert, K., and Boeck, T., 2015. Solutal Marangoni convection in a Hele–Shaw geometry: Impact of orientation and gap width. The European Physical Journal Special Topics, 224(2), 261-276.
34. Assis, T. F., Rojas, E. E. G., Guimarães, G. C., Coelho, M. C., Ramos, A. V., Costa, B. S., & Coimbra, J. S. (2010). Kinematic viscosity and density of binary and ternary mixtures containing hydrocolloids, sodium chloride, and water. International Journal of Thermophysics, 31(3), 513-524.
35. J.D. Jackson: Classical Electrodynamics. John Wiley and Sons, Hoboken, New Jersey, Third edition, 2001.
36. J. Newman and K.E. Thomas-Alyea: Electrochemical Systems. John Wiley and Sons, Hoboken, New Jersey, Third edition, 2004.
37. Young, S.L., Martino, M., Kienzle-Sterzer, C. and Torres, J.A., 1994. Potentiometric titration studies on xanthan solutions. Journal of the Science of Food and Agriculture, 64(1), pp.121-127.
38. Garcıa-Ochoa, F., Santos, V. E., Casas, J. A., & Gomez, E. (2000). Xanthan gum: production, recovery, and properties. Biotechnology advances, 18(7), 549-579.
39. Sworn, G., 2009. Xanthan gum. In Handbook of hydrocolloids (pp. 186-203). Woodhead Publishing.

40. Brown, W. and Mortensen, K., 2014. Scattering in polymeric and colloidal systems. CRC Press.